U.P.B. Sci. Bull., Series A, Vol. 86, Iss. 3, 2034 ISSN 1223-7027

FUSION-BASED ALGORITHM FOR X-RAY PHASE CONTRAST IMAGING TECHNIQUES

Cezara RASINAR*[1,2], Nicoleta SAFCA[2,3], Elena COTORCEANU[2,4], Ionut CIOBANU[1,4], Dan STEFANOIU[1]

Phase Contrast X-ray Imaging represents a technique that has shown remarkable potential in the research field, by providing better visualization of soft tissue, high-contrast images, and high spatial resolution. In the phase contrast imaging technique, the extraction of the three images represented by attenuation, differential phase contrast, and dark-field contrast is essential, providing, in a specific way, information about the nature of the analyzed tissue. This paper introduces a new method based on the three acquired images merging while adjusting the weighting factors, aiming to identify the interest object and to extract the information provided by each contrast channel. In this regard, a fusion-based algorithm was applied to images acquired, using a 5.66 m long Interferometer Talbot-Lau with ultrahigh sensitivity of 0.84 µradians and mean energy of 30 keV. The obtained results are quite promising, as shown in the end of the article.

Keywords: Phase-contrast imaging, grating interferometry, phase-stepping, image fusion algorithm

1. Introduction

In the last decades, X–ray-based imaging techniques have been one of the most widely used tools for medical diagnosis[1], [2]. In conventional radiography techniques, the dominating physical process is represented by the X-ray attenuation effect, which can provide reliable information about high-density materials. At the same time, information regarding soft tissue is neglected. Therefore, as a consequence of the need for soft tissue visualization, researchers have investigated new X-ray-based imaging techniques to overcome the limitations brought by conventional methods [2], [3]. Phase-contrast X-ray imaging has been strongly exploited in the research field [4], [5], exhibiting considerable potential in medical diagnosis, since it provides better visualization for soft tissue due to its sensitivity

---

[1]* Faculty of Automatic Control and Computer Science, National University of Science and Technology POLITEHNICA Bucharest, Romaniae-mail: cezara.rasinar@eli-np.ro (corresponding author)

[2] Extreme Light Infrastructure - Nuclear Physics (ELI-NP), Magurele, Romania

[3] Engineering and Applications of Lasers and Accelerators Doctoral School (SDIALA), National University of Science and Technology POLITEHNICA Bucharest, Romania

[4] Faculty of Chemical Engineering and Biotechnologies, National University of Science and Technology POLITEHNICA Bucharest, Romania

to low atomic number elements [6]. In the last years, a phase-sensitive technique, namely Grating Interferometry has attracted special interest in the research field [7], [8] due to its flexible experimental arrangement and cost-effectiveness. Within this article, the interferometric technique based on the Talbot-Lau interferometer is described [9], [10]. The major strength of this method is that it enables phase-contrast imaging with conventional X-ray tubes, thus showing the increased potential for further implementation in the medical diagnosis field [11]. Also, another important advantage of this new technique is that it yields a visualization of 3 image types or contrast channels (namely, attenuation, phase, and scattering signals) [12], by performing the phase-stepping technique [12]. Moreover, for future implementation in the clinical field, researchers have looked for different ways to design this new concept to meet the requirements of radiologists. Different methods such as Weiner filtering [13], image denoising using wavelets [14], image deconvolution methods for phase retrieval [15], and image-fusion algorithm [16], [17] have been developed for visualization improvements and diagnosis process optimization, in phase-contrast imaging. The fusion-based technique aims to combine the 3 contrast-channel information in a single image, using a different weighting factor for each one, according to the importance of provided information and the need for visualization. The resulting fusion image aims to be not only more meaningful, containing useful information from all 3 images acquired, but also more compatible with clinical requirements, making the evaluation process more accessible [18-20].

This paper introduces a Fourier-based fusion algorithm applied to the 3 images acquired by means of the phase-stepping procedure [21], [22]. In this regard, images were obtained in an X-ray Laboratory, using a Talbot-Lau Interferometer with a high angular sensitivity of 0.84 μrad and a fringe contrast of 14% to 16%. The images were first acquired through the phase-stepping method, then analyzed and processed with the Fourier-based algorithm for the 3-channel extraction, as described in [21] and, finally, merged by using the fusion image method. To prove the effectiveness of the proposed fusion method, images of different chicken organs and tissues were employed. The novelty of the approach described next is represented by the integration of the image-fusion method into a Fourier-based extraction algorithm, followed by the visual evaluation of the informational content that the investigated chicken tissues provide on each channel, and the adjustment of scaling parameters, in order to encompass the features of the analyzed object in a single image.

The article is structured as follows. In the next section, the physical concept of phase-contrast imaging and the grating interferometry technique performed to obtain the images are presented. In section 3, the phase-stepping procedure, the 3 contrast-channel extraction method, and the fusion-based algorithm, developed to enhance the feature visualization and the sharpness of the image are described. The experimental setup is introduced in section 4, while the obtained results of tissues taken from chickens are exhibited in section 5. Some concluding remarks are completing the article.

2. Physical concepts in phase-contrast imaging

It is well known that conventional X-ray imaging methods are based on attenuation effects. However, the phase contrast imaging technique uses the refraction effects and, consequently, the phase change is more important than the attenuation phenomenon [2], [23].

X-rays can be presented through two different perspectives: either as photons or as waves. Mathematically, the oscillation of a complex-valued harmonic, ψ_0, with amplitude $A > 0$ and pulsation $\omega > 0$ is expressed as:

$$\psi_0(t) = A\exp(-\mathrm{j}\omega t), \ \forall t \in \mathbf{R}_+ . \tag{1}$$

Assume the X-ray is propagated through some material (along the Oz axis), as illustrated in Fig. 1. Then, as the figure suggests, the harmonic (1) is distorted by refraction and attenuation phenomena.

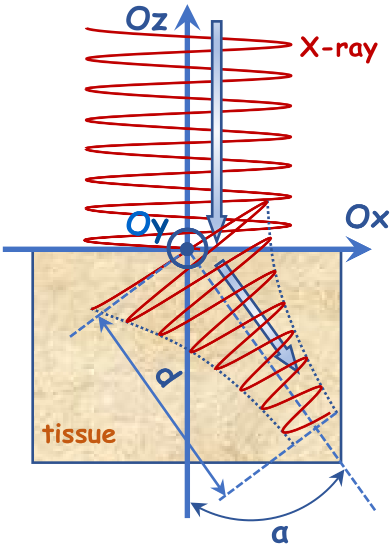

Fig. 1. Refraction and attenuation of an X-ray inside a tissue.

Both phenomena occur along a different direction than Oz axis in 3D space. The angle of this direction, denoted by α, partially depends on the distance traveled by the X-ray inside the tissue. More specifically, if the X-ray has reached some point of coordinates (x, y, z) in tissue, then α only depends on x and y, not on z. Formally, refraction and attenuation effects on X-ray are described by:

$$\psi(d,t) = \psi_0(d,t)\exp(\mathrm{j}nkd) = A\exp\left[\mathrm{j}(nkd - \omega t)\right],\ \forall\, d,t \in \mathbf{R}_+, \tag{2}$$

where $k = 2\pi/\lambda$ is the wave number (depending on wavelength λ), while n is the complex index of refraction, specific to the analyzed tissue. According to [21], [24], this index encompasses both effects: refraction (or the elastic effect) in the real part and attenuation (or the inelastic effect) in the imaginary part, as expressed below [25]:

$$n = 1 - \delta + \mathrm{j}\beta. \tag{3}$$

In Eq. (3), δ is the refraction index and β is the attenuation index. Both depend on the position of the current point inside the tissue, (x,y,z). With Eq. (3), the distorted X-ray (2) becomes:

$$\psi(d,t) = \underbrace{A\exp(-kd\beta)}_{|\psi(d,t)|}\exp\left\{\mathrm{j}\left[kd(1-\delta) - \omega t\right]\right\},\ \forall\, d,t \in \mathbf{R}_+. \tag{4}$$

In Eq. (4), one can easily notice how the amplitude of genuine X-ray is attenuated (by an exponential law), whereas its phase shift is caused by refraction. Focus now on phase, as it represents the main contrast mechanism for the presented imaging technique. The phase variation can be evaluated like in [23] and [24]:

$$\Delta\phi(x,y) = k\int \delta(x,y,z)dz \tag{5}$$

and does not depend on the depth of propagation (as the integral is computed along the Oz axis, which is the initial propagation direction of the X-ray). The refraction angle is strongly related to the first derivative of the phase shift along Ox axis [11],[24]:

$$\alpha(x,y) = \frac{1}{k}\frac{\partial\Delta\phi}{\partial x}(x,y) = \int \frac{\partial\delta}{\partial x}(x,y,z)dz \tag{6}$$

Analyzing the phenomenon caused by the X-ray interaction with matter, some studies (e.g. [11], [23-24]) employed different types of weakly absorbing materials, showing that the refractive index decrement is about 3 orders greater than the absorption (attenuation) index, for the clinical energy range (of 10-100 keV). Another important aspect is represented by their dependence on the energy E: δ decreases more slowly, with E^{-2}, whereas the decay of β is approximatively proportional to E^{-4} [11], [26]. This observation enables increasing the energy without reducing the contrast. Consequently, the X-ray phase shift contribution is expected to be more effective than attenuation in obtaining high contrast for soft tissue density variations in the human body.

In this regard, researchers designed different techniques that provide phase-contrast images, aiming to improve the visualization of internal structures and reduce the radiation dose for patients. Various methods that have been developed, can be categorized as follows: Analyzer-Based Imaging (ABI)[26], Crystal Interferometry (CI)[27], Propagation-Based Imaging (PBI)[28], Grating Interferometry (GI)[29], and the non-interferometric methods [30][31]. The technique proposed in this article is represented by the GI, consisting of 3 periodic gratings that provide high phase sensitivity [32-34].

3. Methods of interferometric imaging

In this section, the theoretical foundations regarding the interferometric imaging technique and the image-acquiring methods, followed by the processing algorithms employed to improve visualization are presented.

3.1. Grating Interferometry method

The GI method, employed in this article, is based on a Talbot-Lau Interferometer with high angular sensitivity [35], used together with a polychromatic source. The interferometer performance is described by the contrast or fringe visibility and the angular sensitivity. The latter represents the smallest measurable refraction angle and in this paper is defined as by the ratio between the grating period and the inter-grating distance.

The components of the Talbot-Lau interferometer and their contribution to phase-contrast image formation are described next, with the help of Fig. 2. As illustrated, the set-up consists of three gratings, with the same period (of micrometric order), an X-ray source and a detector.

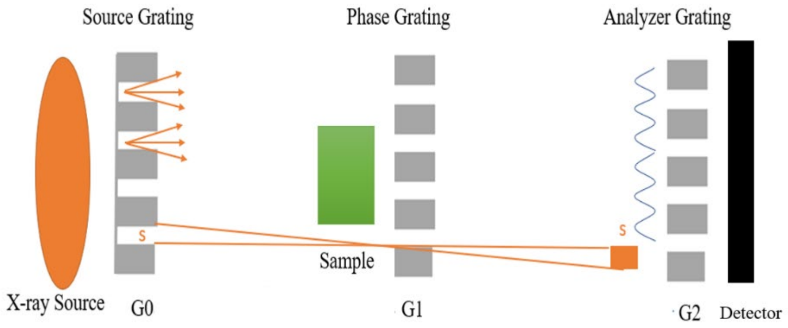

Fig. 2. Grating Interferometry experimental set-up, consisting of 3 micro-periodic gratings, an X-ray source and a detector. The extended source size is shaped into an array of fine slit sources, by using a source grating (G0). This aspect fulfills the special requirement for transverse coherence of the wavefront. This way, each virtual source *s* contributes to create an interference pattern with good contrast at the analyzer plane because of sufficient spatial coherence.

The phase grating G1 is used to split the transmitted X-ray beam in $\pm 1^{st}$ diffraction orders, that interfere and produce a periodic interference pattern [21]. An object (sample) is positioned between the source grating and the phase grating, near the G1, producing a displacement of the interference pattern [21], [36]. Since the resulting fringe pattern has a period of only a few micrometers, the existing detectors cannot directly resolve it. Thus, the analyzer grating G2 was introduced, to match the period of the interference pattern and to transform the fringe positions into intensity variations [21], [36]. Additionally, a source grating G0 is placed between the object and the X-ray source, aiming to ensure beam coherence, which is a requirement for the appearance of the interference pattern [28], [36-37].

By operating this system and performing a phase-stepping procedure, images are acquired. Three contrast parameters are extracted for images, namely: the attenuation, the differential phase (or the refraction angle), and the scattering. By means of phase-stepping procedure, nearly sinusoidal intensity modulations are recorded in each pixel. Such modulations can be analyzed to extract information about the 3 parameters. For each pixel, the attenuation is obtained from the mean value of the intensity oscillation, the phase gradient is obtained from the phase difference of intensity oscillation, while scattering is defined as a change in the amplitude of the intensity oscillation. The scattering is associated to the visibility of the stepping curve. (The computing equations of all 3 parameters are written in the next sub-section.) By gathering the values of a contrast parameter from all pixels, a new image is obtained. Thus, 3 images can characterize the contrast of each analyzed image: the attenuation image, the differential phase contrast image, and the scattering image (also referred to as dark-field image). Afterwards, the *2D Discrete Fourier Transform* (2D-DFT) is applied to every one of the 3 contrast images [22]. Thus, their information is represented in the frequency domain, which will facilitate obtaining one single fusion image with better contrast, as described in sub-section 3.3.

Two types of scans are used: the reference one, without the object in the interference pattern, and the one with the investigated object in the beam path [36].

3.2. Phase-stepping procedure and contrast parameters extraction

For data collection and analysis, a phase-stepping procedure is performed, which consists of scanning the source grating (G0) at a certain number of positions (e.g. 16 positions) or steps. This method relies on the assumption that an object positioned in the beam will determine the shift of the intensity pattern that can be translated into fringe pattern modulations [7], [37].

The grating scan varies the transmission of the interferometer as a function of the deviation angle, producing in each detector pixel a nearly sinusoidal intensity modulation curve [11].

The 3 contrast parameters are computed according to the principle illustrated in Fig. 3 [21].

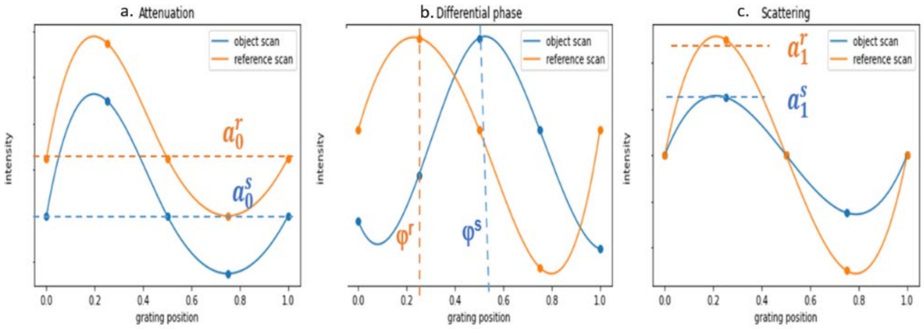

Fig. 3. Intensity oscillation curve obtained for each signal of X-rays: attenuation (a), differential phase (b), and scattering(c), for each pixel.

Assume that the image matrix has N rows and M columns. Consider the current pixel located at coordinates (n,m), with $n \in \overline{1,N}$ and $m \in \overline{1,M}$. Then, the relative intensity of pixel attenuation can be computed as follows:

$$I_{\text{att}}[n,m] = \frac{a_0^s[n,m]}{a_0^r[n,m]}, \quad (7)$$

where a_0^s and a_0^r are the intensity average values for the scan with object and the reference scan, respectively. Practically, as Fig. 3 suggests, a_0^s and a_0^r are the two characteristic biases of the harmonic intensity.

The intensity corresponding to differential phase is:

$$I_{\text{phase}}[n,m] = \varphi^s[n,m] - \varphi^r[n,m], \quad (8)$$

where φ^s and φ^r are the phase of harmonic intensity in both scan types. Obviously, when the object to scan is present, the harmonic is delayed, compared to the case when no object was inserted between gratings.

The intensity of scattering resulting image can be evaluated by:

$$I_{\text{scatt}}[n,m] = \frac{a_1^s[n,m]}{a_1^r[n,m] I_{\text{att}}[n,m]}, \quad (9)$$

where a_1^s and a_1^r are the oscillation amplitude for the two types of scans, respectively. The inserted object causes not only attenuation of the X-ray, but also a phase change.

From the 3 contrast images, the X-ray interaction with matter tendency influences the information provided by each contrast image. For example, while the material is strong scattering, the differential phase contrast image would present poor signal. By fusing parts from all 3 images, superior image with good contrast should be obtained.

3.3. Image fusion algorithm based on Fourier Transform

After obtaining the 3 images, a fusion procedure should be applied. One aims to obtain a single image that combines the information from all 3 images above [18], [19], [35]. In order to keep the fusion procedure as simple as possible, all images have squared shape (i.e. the number of rows equals the number of columns).

The fusion method consists of 4 main steps (see [16], [18], [20]):

1. First, the 2D-DFT is applied to each contrast image to obtain the corresponding frequency representation. In this way, the information of each image is mainly concentrated in the middle of resulted matrices with complex values (where the low frequencies lie).
2. Next, the complex matrices are weighted by 2D Gaussian bells centered in the middle. Their role is to increase even more the importance of low frequency zone comparing to the high frequency zones (where, usually, the information is corrupted by various noises). Actually, the Gaussian bell is a filter that denoises the important information about the contrast. (At least the differential phase contrast image requires denoising.)
3. The third step is the most important. Here, the three filtered matrices are linearly combined, with the help of some variable weights, to obtain a single fusion matrix. The weights can be set according to the analyzed object characteristics and frequency behavior of contrast matrices.
4. The inverse 2D-DFT is applied at the fourth step to the fusion matrix. This produces the fusion image, which is expected to have better contrast and to emphasize more details than any of the initial images.

Each step is explained next at length.

Recall that, if $\mathbf{A}$ is a square image matrix of size $N \times N$ (usually with pixel intensity varying between 0 and 1), the 2D-DFT can be computed as below:

$$F_{\mathbf{A}}[kr,kc] = \sum_{nr=0}^{N-1} \sum_{nc=0}^{N-1} A[nr,nc] \exp\left(-\mathrm{j} \frac{2(nr \cdot kr + nc \cdot kc)\pi}{N} \right), \quad \forall\, kr,kc \in \overline{0,N-1}. \quad (10)$$

In Eq. (10), $A[nr,nc]$ is the current element of matrix $\mathbf{A}$ (the current pixel intensity, assuming the indexing starts from 0), while $F_{\mathbf{A}}[kr,kc]$ is the Fourier coefficient for frequency indexes kr and kc. The matrix that gathers all Fourier coefficients is $\mathbf{F}_{\mathbf{A}}$ and can be organized such that the low frequency information falls into the middle (around the coordinates $(N/2, N/2)$), by accounting the symmetry properties of Fourier Transform.

The inverse 2D-DFT is:

$$A[nr,nc] = \sum_{kr=0}^{N-1}\sum_{kc=0}^{N-1} F_{\mathrm{A}}[kr,kc]\exp\left(\mathrm{j}\frac{2(nr\cdot kr + nc\cdot kc)\pi}{N}\right),\quad \forall\, nr,nc \in \overline{0,N-1}. \qquad (11)$$

After applying the transform (10) to the image matrices $\mathbf{I}_{\mathrm{att}}$, $\mathbf{I}_{\mathrm{phase}}$ and $\mathbf{I}_{\mathrm{scatt}}$, one obtains the frequency matrices simply denoted by $\mathbf{F}_{\mathrm{att}}$, $\mathbf{F}_{\mathrm{phase}}$ and $\mathbf{F}_{\mathrm{scatt}}$, respectively. All matrices are of size $N \times N$. This allows building the 2D Gaussian bell straightforwardly. The central point is $\mu = N/2$, while the standard deviation σ can be computed by considering that the frequency matrix is covered by the 6σ-interval. More specifically, $\sigma = (N-1)/6$. Thus, the generic 2D Gaussian bell is expressed as:

$$G(x,y) = \frac{1}{2\pi\sigma^2}\exp\left[-\frac{(x-\mu)^2+(y-\mu)^2}{2\sigma^2}\right],\quad \forall\, x,y \in \mathbf{R}. \qquad (12)$$

The bell (12) needs to be sampled, in order to make possible multiplication with frequency matrices. Thus, the Gaussian matrix to employ is $\mathbf{G}$ and its generic element can be computed by:

$$G[n,m] = \frac{1}{2\pi\sigma^2}\exp\left[-\frac{(n-\mu)^2+(m-\mu)^2}{2\sigma^2}\right],\quad \forall\, n,m \in \overline{1,N}. \qquad (13)$$

The elementwise multiplication between the matrix $\mathbf{G}$ and matrices $\mathbf{F}_{\mathrm{att}}$, $\mathbf{F}_{\mathrm{phase}}$, $\mathbf{F}_{\mathrm{scatt}}$ leads to filtered frequency matrices $\mathbf{F}^{\mathbf{G}}_{\mathrm{att}}$, $\mathbf{F}^{\mathbf{G}}_{\mathrm{phase}}$, $\mathbf{F}^{\mathbf{G}}_{\mathrm{scatt}}$, respectively. A single fusion matrix can be obtained from the filtered matrices, by means of linear combination below:

$$\mathbf{F}^{\mathbf{G}} \equiv w_{\mathrm{att}}\mathbf{F}^{\mathbf{G}}_{\mathrm{att}} + w_{\mathrm{phase}}\mathbf{F}^{\mathbf{G}}_{\mathrm{phase}} + w_{\mathrm{scatt}}\mathbf{F}^{\mathbf{G}}_{\mathrm{scatt}}, \qquad (14)$$

where w_{att}, w_{phase} and w_{scatt} are corresponding weights that have to be set. Setting them as constants proved to be unrealistic, because each object has some refraction and absorption characteristics at X-rays. Thus, constant weights can lead to a modest fusion contrast image. Therefore, the weights have to be set by accounting both the natural inner structure of analyzed object and the frequency behavior of contrast matrices. In [20], the authors propose an interesting adaptive assignment of weights, based on frequency approach.

The normalized frequency plane can be split into K squared frequency sub-bands, like in Fig. 4. The normalized frequencies are fr (for matrix rows) and fc (for matrix columns).

According to the frequency structure above, the weights can be set to be constant at each sub-band level, while varying from a sub-band to another. More specifically, for each $k \in \overline{1,K}$:

$$w_{\mathrm{att}} = \frac{K^2}{K^2 + c_{\mathrm{att}} k^2}, \quad w_{\mathrm{phase}} = \frac{c_{\mathrm{phase}} k^2}{K^2 + k^2}, \quad w_{\mathrm{scatt}} = \frac{c_{\mathrm{scatt}} k^2}{K^2 + k^2}, \tag{15}$$

where c_{att}, c_{phase} and c_{scatt} are constants to be determined depending on the object characteristics. Fig. 5 exhibits the variation of weights (15), for $K = 100$, $c_{\mathrm{att}} = 0.3$, $c_{\mathrm{phase}} = 1$ and $c_{\mathrm{scatt}} = 2$.

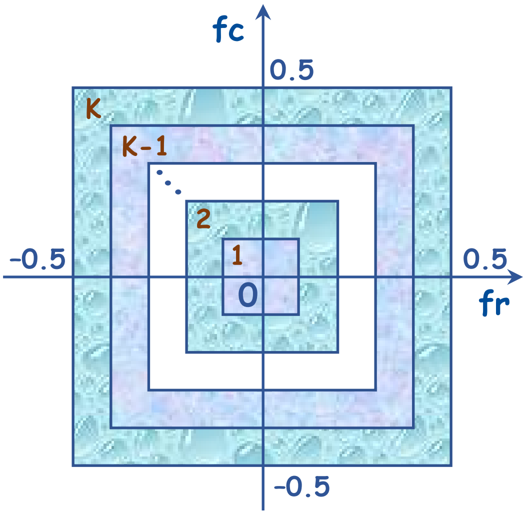

Fig. 4. Splitting the normalized frequency plane into sub-bands.

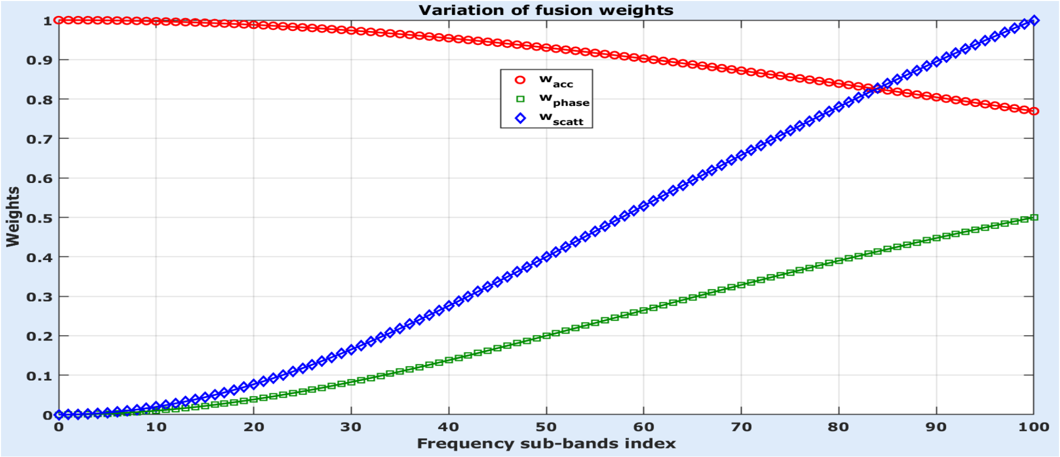

Fig. 5. Variation of fusion weights, depending on frequency sub-bands index.

One can easily observe that, as the frequency sub-band index increases, the weight for the attenuation image decreases, while for differential phase contrast and scattering images, the weights increase. This means the information of attenuation image is dominant at low frequency, whereas phase and scattering bring more information at high frequency. Hence, the attenuation is responsible for creating the zones with small variations in pixels intensities (quite constant grey level), while the phase and scattering bring to the fusion image information about contours, lines, curves etc., where pixels intensity exhibit rapid variations or even jumps.

The only problem left is to set the constants K, c_{att}, c_{phase} and c_{scatt}. Unfortunately, there is no general rule for setting them, because they strongly depend on the molecular structure of tissue to analyze. Therefore, usually, the constants are semi-empirically determined, in a subjective manner. Thus, several combinations of constants are tested and the results on the final fusion image are visually compared. The combination that leads to the fusion image with the best visual contrast is selected. This means fulfilling two major goals: noise reduction and sharpness enhancement into the fusion image.

Setting K is easier than setting the other 3 constants, since the experiments revealed that increasing the number of sub-bands beyond 10 does not improve much the quality of fusion image. Consequently, for each K varying from 0 to 10 (where 0 means without sub-bands), the best constants c_{att}, c_{phase} and c_{scatt} can be found. The final assessment is to select the best combination out of the 11 ones.

At the final step, the inverse 2D-DFT (11) has to be applied on fusion matrix (14). Thus, the fusion image $\mathbf{I}^{\mathbf{G}}$ is obtained.

4. Experimental setup

Based on the interferometer introduced in [35], a similar symmetrical Talbot-Lau Interferometer has been employed to perform experiments. The interferometer has an angular sensitivity of 0.84 µrad and an average visibility of around 14%, being placed within the X-ray imaging laboratory, from ELI-NP. The system is composed of a conventional X-ray tube, three micro-periodic gratings, and a high-resolution detector, as illustrated in Fig. 6.

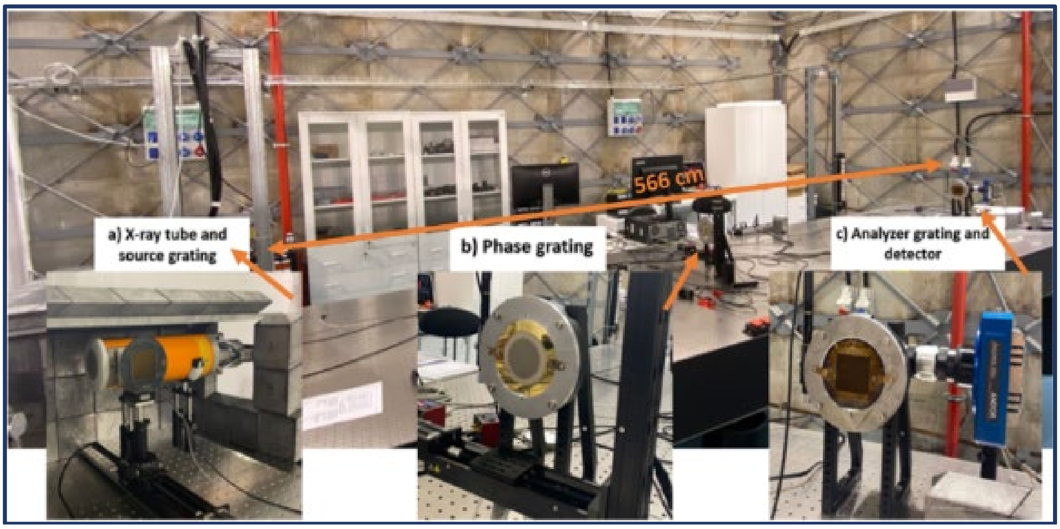

Fig. 6. Photo of Talbot-Lau Interferometer from the X–ray Imaging Laboratory from ELI-NP.

The X-ray source is a conventional tungsten anode tube, having a 400 µm focal spot operated at 30 kVp. The interferometer is 566 cm long and consists of three micro-periodic gratings that were designed to have the smallest constant period, of 2.4 µm for the mean energy of 25 keV (which corresponds to a wavelength of 0.049 nm) [12]. The two absorbing gratings, namely the source grating and the analyzer grating, present a nominal thickness of 60 µm gold, while the employed phase grating is 8 µm thick and made of nickel. The detector consists of a CsI scintillator and a CCD Camera with a pixel size of 12×12 µm, placed at 566 cm from the source, next to the analyzer grating.

The setup configuration is symmetrical, as the phase grating (G1) is positioned midway between the source grating (G0) and the analyzer grating (G2). As Fig. 6 illustrates, the source grating is placed in front of the X-ray source, while the analyzer grating is placed in front of the detector.

The objects to be analyzed during the experiments are represented by different types of chicken tissue embedded in recipients containing water, as shown in Fig. 7. These conditions help avoiding the phase variations that can arise at the interface between tissue and air.

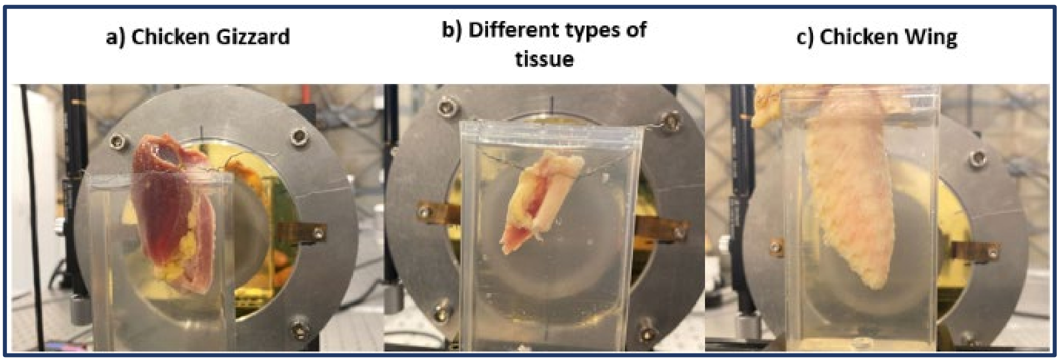

Fig. 7. Three objects used in experiments: a) Chicken Gizzard; b) Different types of tissue (namely: bone, muscle, and adipose matter); c) Chicken Wing.

First, the chicken gizzard was analyzed, as it consists of muscles and connective tissue. Then, an object that comprises different types of chicken tissue, such as bone, muscle, and adipose matter was tested. Finally, a chicken wing was exposed to the X–ray beam.

The images are obtained using the previously described setup, operated at 30 keV mean energy and 10 mA intensity. Then, a set of 16 images is acquired using the phase–stepping procedure, in which the source grating is translated in 16 steps, of 0.3 µm, over two periods of the grating. The exposure time for each imagine from the set is 80 seconds. After performing the phase-stepping procedure, the contrast parameters are determined as described in sub-section 3.2, and the 3 images are obtained. Next, the 4-step fusion algorithm of sub-section 3.3 was run.

5. Experimental results

By performing the phase-stepping procedure, a dataset of 16 images is acquired for each investigated sample. In Fig.8, three images of the dataset are illustrated. As the performed steps are very small, it is hard to observe some differences between these three images. This method causes intensity modulations in each pixel to be recorded, and the three signals are extracted by performing the Fourier Analysis of the phase stepping curve. Thus, the three images are obtained: attenuation, phase, and scattering.

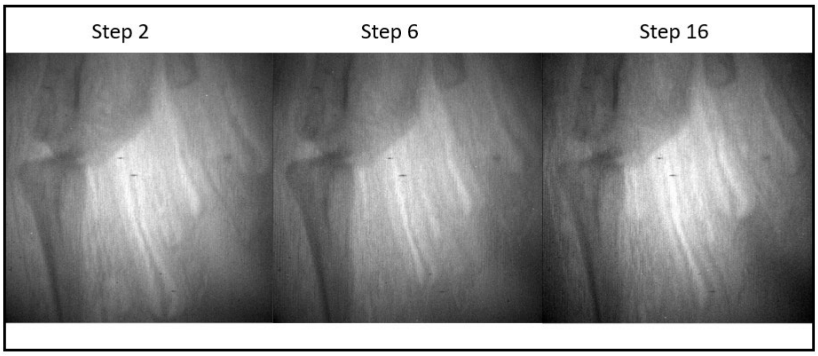

Fig.8. Images acquired through the phase stepping procedure, corresponding to step 2, 6, ang 16 respectively

In the following figures, 4 images are shown, from left to right: attenuation, differential phase contrast, scattering, and fusion. For all 3 tested objects, the 3 contrast images (attenuation, differential phase and scattering) are obtained performing the phase-stepping procedure of 16 steps with 80 seconds per step, at 30 kVp and 10 mA intensity.

In Fig. 9, the results for chicken gizzard are displayed.

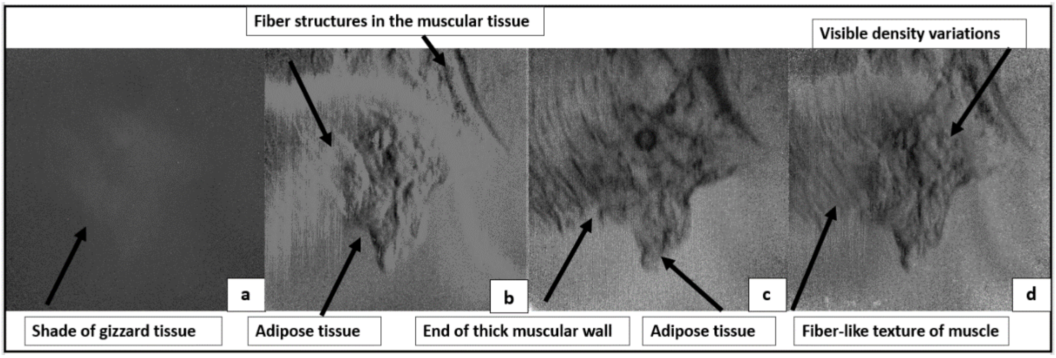

Fig. 9. Experimental results for a chicken gizzard. a. attenuation image; b. differential phase contrast image; c. scattering image; d. fusion image.

The most suitable frequency plane splitting was in $K = 10$ sub-bands, for which the best-found weighting constants corresponding to each contrast parameter are: $c_{\text{att}} = 1$, $c_{\text{phase}} = 3$ and $c_{\text{scatt}} = 6$.

The attenuation image in Fig. 9a exhibits low contrast and poor informational content concerning the local details, as expected. A shade of the investigated object can slightly be noticed. However, this image is important for creating the overall background of the fusion image. The differential phase contrast image in Fig. 9b shows the fiber-like texture of the thick muscle in the gizzard. The extracted scattering image in Fig. 9c is the most significant, providing more information about small density variations in the adipose and muscular tissue, which are known as strongly scattering materials.

Because the attenuation image provides low-contrast content and its contribution is almost insignificant, it was suitable to neglect the low frequency information and rather use the high frequency sub-bands. In this case, the scattering image presents enhanced visibility and more information about both the fibrous and adipose tissue of the gizzard, compared to the differential phase contrast image, which shows about the same visible artifacts, but affected by sensibly higher noise. This is the reason for setting the constants of the weighting as previously mentioned. When looking at the fusion image in Fig 9d, one can see that, on one hand, the noise was reduced (especially comparing to the differential phase contrast and scattering images) and, on the other hand, the sharpness was increased, allowing easier identification of various structures inside the gizzard tissue.

The second object to analyze includes a combination of three different types of tissue: bone, muscle, and fat from different chicken organs. Thus, one aims to balance the contribution of each contrast channel into the fusion image.

The experimental results are displayed in Fig. 10.

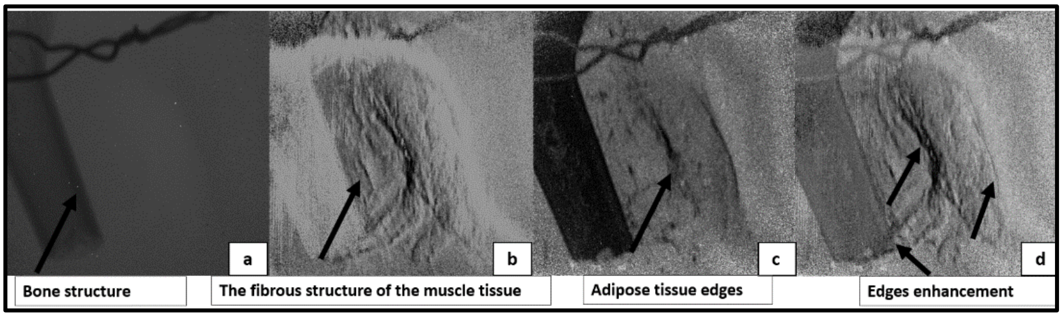

Fig. 10. Experimental results for three different types of tissue: bone, muscle, and adipose matter. a. attenuation image; b. differential phase contrast image; c. scattering image; d. fusion image.

Like in the previous experiment, the number of sub-bands was set to $K = 10$. The best corresponding constants resulted to be: $c_{\text{att}} = 1$, $c_{\text{phase}} = 5$ and $c_{\text{scatt}} = 4$.

As illustrated in Fig. 10a, the attenuation image provides significant information about the bone structure and lack of information about the muscle and adipose tissue. The differential phase contrast image in Fig. 10b exhibits poor signal quality (quite noisy) for the investigated bone, due to the strong absorption tendency of the high-density material. However, due to the refracting tendency of the material, the enhancement of the fibrous structure of the muscle is noticed. The scattering signal in Fig. 10c provides better margin delineation (contour emphasizing) and small differences in density variations of the strongly scattering adipose tissue, although the information about the bone is too strong, to the detriment of the other tissues. Therefore, the highest constant was set for differential image, closely followed by the constant for scattering image.

The object used in the last experiment, shown in Fig. 11, is represented by a chicken wing, consisting of bone, muscle, and skin.

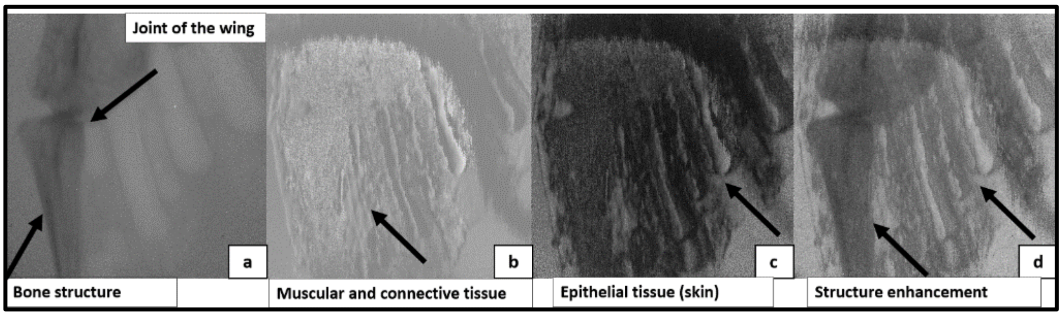

Fig. 11. Experimental results for a chicken wing. a. attenuation image; b. differential phase contrast image; c. scattering image; d. fusion image.

This time, the number of sub-bands was set to $K = 5$ and the working constants are: $c_{\text{att}} = 5$, $c_{\text{phase}} = 1$ and $c_{\text{scatt}} = 4$.

Since the object is composed of different types of tissue, one expects that the 3 images provide different information. One can see the clear structure of the chicken bone in the attenuation image of Fig. 11a. At the same time, there is a lack of information about the high-density matter, in the differential phase contrast and scattering images. As noticed in Fig. 11b, the differential phase contrast image displays different textural features of the connective tissue, but the signal quality is poor due to the strong scattering tendency of the epithelial tissue. Therefore, the scattering image in Fig. 11c renders significant information about the small density differences in the tissue. All these observations led to the necessity to increase the attenuation coefficient, which lowers the contribution of corresponding image at high frequency in the fusion image of Fig. 11d. Since the phase coefficient is small, the dominant contribution at high frequency is made by the scattering image.

The milestone of image fusion method is represented by the evaluation of the best weights to combine the information from the 3 contrast images in a single fusion image with lesser noise and better sharpness. As the first and second investigated objects revealed, the visibility of the soft tissue features and edge-enhancement was improved, by using increased scaling weights for the differential phase contrast and scattering images. The last example showed that good contrast of fusion image is obtained when using both low and high frequency components. All three experiments have proven that knowing in advance the absorption, refraction and scattering properties of the analyzed tissue can help finding the best combination of weights to build the fusion image.

6. Concluding remarks and future approaches

The aim of this article was to design and implement a fusion-based algorithm for X-ray phase contrast images, that provides a new visualization approach, improving the identification process of the interest object. To obtain the desired images, a Talbot-Lau Interferometer was employed, with an ultrahigh sensitivity of 0.84 µrad. Three objects, consisting of different types of tissue, have been investigated. Images collected through the phase-stepping method were later processed, resulting in three contrast images: attenuation, differential phase contrast and scattering. To build superior fusion images (denoised and with better sharpness), visual detection of the features provided by the three composing images, as well as the intrinsic properties of analyzed tissue (especially absorption, refraction, and scattering) are very important. This allows setting the number of frequency sub-bands as well as the weights to be applied for each sub-band.

The experimental results have shown significant improvements in merging the individual content of each signal with different percentages, in visualizing the object features, edge enhancement, and structural characteristics of tissue. Furthermore, this method has shown improved results in terms of image sharpness, noise reduction, and complexity of the image. Finally, the proposed method provides valuable capability to render the biological characteristics of different tissue types. Also, from a diagnostic point of view, the method presents a meaningful potential to provide useful information, depending on the necessity of investigation. Through this method, the experts would be able to set the parameters needed for an advantageous visualization and deliver a reliable diagnosis. Furthermore, the fusion-based algorithm can be adapted to various types of image. For example, one can employ reconstructed images acquired through a novel tomosynthesis-based algorithm for phase contrast mammographic images.

The image fusion algorithm can be improved in at least two respects. Firstly, it would be better to define a cost function to optimize, in order to select the number of frequency sub-bands and the three weighting constants. In this way, their determination becomes less subjective and less empirical. Moreover, the cost function can be optimized through a metaheuristic. Secondly, a different transform than the Fourier's one could be employed. Any transform from the time-frequency-scale class can constitute a good candidate. For example, the Wavelet Transform is of worth to be considered, as wavelets have the capacity to focus on contours and boundaries between various textures inside the image. Least, but not last, a user-friendly interface can be designed and implemented to facilitate running the algorithm.

Acknowledgments

This work was carried out under the contract PN 23 21 01 06 sponsored by the Romanian Ministry of Research, Innovation, and Digitalization; supported by ELI-NP project – Phase II, co-financed by the Romanian Government and the European Union through the European Regional Development Fund: the Competitiveness Operational Program (1/07.07.2016, C.O.P., ID 1334).

REFERENCES

[1] *S. A. Zhou and A. Brahme*, "Development of phase-contrast X-ray imaging techniques and potential medical applications", Physica Medica, vol. 24, no. 3, pp. 129–148, 2008, doi: 10.1016/j.ejmp.2008.05.006.

[2] *A. Bravin, P. Coan, and P. Suortti*, "X-ray phase-contrast imaging: From pre-clinical applications towards clinics", Physics in Medicine and Biology, vol. 58, no. 1, pp. 1-35, Jan. 07, 2013, doi: 10.1088/0031-9155/58/1/R1.

[3] *A. Momose, T. Takeda, Y. Itai, and K. Hirako*, "Phase-contrast X-ray computed tomography for observing biological soft tissues", Nat. Med., vol. 2, no. 4, pp. 473–475, 1996, doi: 10.1038/nm0496-473.

[4] *D. M. Paganin and D. Pelliccia*, "X-ray phase-contrast imaging: A broad overview of some fundamentals", in Advances in Imaging and Electron Physics, Academic Press Inc., vol. 218, pp. 1–158, 2021, doi: 10.1016/bs.aiep.2021.04.002.

[5] *A. Olivo*, "Edge-illumination X-ray phase-contrast imaging", Journal of Physics Condensed Matter, IOP Publishing Ltd, vol. 33, no. 36, article 363002, Sep. 01, 2021, doi: 10.1088/1361-648X/ac0e6e.

[6] *L. Quenot, S. Bohic, and E. Brun,* "X-ray Phase Contrast Imaging from Synchrotron to Conventional Sources: A Review of the Existing Techniques for Biological Applications", Applied Sciences (Switzerland), vol. 12, no. 19, article 9539, Oct. 01, 2022, doi: 10.3390/app12199539.

[7] *T. Thuering and M. Stampanoni*, "Performance and optimization of X-ray grating interferometry", Philosophical Transactions of the Royal Society A: Mathematical, Physical and Engineering Sciences, vol. 372, article 20130027, Mar. 2014, doi: 10.1098/rsta.2013.0027.

[8] *J. Vila-Comamala et al.,* "High sensitivity X-ray phase contrast imaging by laboratory grating-based interferometry at high Talbot order geometry", Opt. Express, vol. 29, no. 2, pp. 2049- 2064, Jan. 2021, doi: 10.1364/oe.414174.

[9] *A. Gustschin et al.*, "High-resolution and sensitivity bi-directional X-ray phase contrast imaging using 2D Talbot array illuminators", Optica, vol. 8, no. 12, pp. 1588-1595, Dec. 2021, doi: 10.1364/optica.441004.

[10] *N. Morimoto et al.*, "Talbot-Lau interferometry-based X-ray imaging system with retractable and rotatable gratings for nondestructive testing", Review of Scientific Instruments, vol. 91, no. 2, article 023706, Feb. 2020, doi: 10.1063/1.5131306.

[11] *N. Safca, P. Ghenuche, C. A. Ur, and D. Stutman*, "Perspective on using Talbot-Lau X-ray phase contrast imaging for atherosclerosis diagnosis", Scientific Bulletin of UPB, Series A: Applied Mathematics and Physics, vol. 83, no. 3, pp. 257–266, 2021.

[12] *T. E. Gureyev et al.*, “Dark-field signal extraction in propagation-based phase-contrast imaging”, Phys. Med. Biol., vol. 65, no. 21, article 215029, Nov. 2020, doi: 10.1088/1361-6560/abac9d.

[13] *S. Gong, F. Gao, and Z. Zhou*, “Improving visibility of X-ray phase-contrast imaging with Wiener filtering”, J. X-Ray Sci. Technol., vol. 18, no. 3, pp. 279–292, 2010, doi: 10.3233/XST-2010-0260.

[14] *C. Arboleda, Z. Wang, and M. Stampanoni*, “Wavelet-based noise-model driven denoising algorithm for differential phase contrast mammography”, Opt. Express, vol. 21, no. 9, pp. 10572-10589, May 2013, doi: 10.1364/oe.21.010572.

[15] *A. Olivo and R. D. Speller*, “Deconvolution of X-ray phase contrast images as a way to retrieve phase information lost due to insufficient resolution”, Phys. Med. Biol., vol. 54, no. 15, article N347, 2009, doi: 10.1088/0031-9155/54/15/N02.

[16] *Eduardo Coello*, “Fourier domain image fusion for differential X-ray phase-contrast breast imaging”, Eur. J. Radiol., vol. 89, pp. 27–32, Apr. 2017.

[17] *H. Liu et al.*, “Multimodal image fusion for X-ray grating interferometry”, Sensors, vol. 23, no. 6, article 3115, 2023, doi: 10.3390/s23063115.

[18] *J. I. Sperl, D. Bequé, G. P. Kudielka, K. Mahdi, P. M. Edic, and C. Cozzini*, “A Fourier-domain algorithm for total-variation regularized phase retrieval in differential X-ray phase contrast imaging”, Opt. Express, vol. 22, no. 1, pp. 450-462, 2014, doi: 10.1364/oe.22.000450.

[19] *M. Stampanoni et al.*, “Toward clinical differential phase contrast mammography: Preliminary evaluations and image processing schemes”, Journal of Instrumentation, vol. 8, no. 5, article C05009, 2013, doi: 10.1088/1748-0221/8/05/C05009.

[20] *Z. Wang et al.*, “Image fusion scheme for differential phase contrast mammography”, Journal of Instrumentation, vol. 8, article C07011, Jul. 2013. doi: 10.1088/1748-0221/8/07/C07011.

[21] *A. Sarapata*, “Quantitative X-ray imaging with high-energy grating interferometry at Conventional Sources”, Dissertation Thesis, Technical University of Munich, July 2015.

[22] *J. Dittmann, A. Balles, and S. Zabler*, “Optimization based evaluation of grating interferometric phase stepping series and analysis of mechanical setup instabilities”, J. Imaging, vol. 4, no. 6, article 77, 2018, doi: 10.3390/jimaging4060077.

[23] *X. Wu and H. Liu*, “Clinical implementation of X-ray phase-contrast imaging: Theoretical foundations and design considerations”, Med. Phys., vol. 30, no. 8, pp. 2169–2179, 2003, doi: 10.1118/1.1593836.

[24] *D. Stutman, T. J. Beck, J. A. Carrino, and C. O. Bingham*, “Talbot phase-contrast X-ray imaging for the small joints of the hand,” Phys. Med. Biol., vol. 56, no. 17, pp. 5697–5720, 2011, doi: 10.1088/0031-9155/56/17/015.

[25] *Als-Nielsen J and McMorrow D* 2001 Elements of Modern X-Ray Physics (Chichester: Wiley)

[26] *Wang, Zhili and Liu, Dalin and Zhang, Jin and Huang, Wanxia and Yuan, Qingxi and Gao, Kun and Wu, Zhao*, “Absorption, refraction and scattering retrieval in X-ray analyzer-based imaging”, Journal of Synchrotron Radiation, vol. 25, no.4, pp. 1206-1213, 2018, doi: 10.1107/S1600577518007439.

[27] *Yoneyama, Akio and Takamatsu, Daiko and Lwin, Thet-Thet and Yamada, Shigehito and Takakuwa, Tetsuya and Hyodo, Kazuyuki and Hirano, Keiichi and Takeya, Satoshi*, Crystal-Based X-ray Interferometry and Its Application to Phase-Contrast X-ray Imaging, Zeff Imaging, and X-ray Thermography, Applied Sciences, vol. 13, no. 9, article 5424, 2023, doi: 10.3390/app13095424.

[28] *Gradl, R., Dierolf, M., Hehn, L. et al.* Propagation-based Phase-Contrast X-ray Imaging at a Compact Light Source. *Sci Rep*, vol. 7, is. 1, article 4908, 2017, doi: 10.1038/s41598-017-04739-w.

[29] *P. Modregger and B. R. Pinzer and T. Thüring and S. Rutishauser and C. David and M. Stampanoni,* Sensitivity of X-ray grating interferometry, Opt. Express, vol. 19, no. 19, pp 18324—18338, 2011, doi: 10.1364/OE.19.018324.

[30] *M. Endrizzi, P. Diemoz, Peter Munro, C. Hagen1, M. B. Szafraniec1, T. P. Millard1, C. E. Zapata, R. D. Speller and A. Olivo*, Applications of a non-interferometric x-ray phase contrast imaging method with both synchrotron and conventional sources, Journal of Instruments, vol. 8, no. 5, pp C05008, 2018, doi: 10.1088/1748-0221/8/05/C05008

[31] *M. Endrizzi,* "X-ray phase-contrast imaging", Nuclear Instruments and Methods in Physics Research, Section A: Accelerators, Spectrometers, Detectors and Associated Equipment, Elsevier B.V., vol. 878. pp. 88–98, Jan. 11, 2018, doi: 10.1016/j.nima.2017.07.036.

[32] *E. Eggl et al.*, "Dose-compatible grating-based phase-contrast mammography on mastectomy specimens using a compact synchrotron source", *Sci. Rep.*, vol. 8, no. 1, article 15700, Dec. 2018, doi: 10.1038/s41598-018-33628-z.

[33] *H. Itoh, K. Nagai, G. Sato, K. Yamaguchi, T. Nakamura, T. Kondoh, C. Ouchi, T. Teshima, Y. Setomoto, and T. Den,* "Two-dimensional grating-based X-ray phase-contrast imaging using Fourier transform phase retrieval," Opt. Express, vol. 19, article 3339-3346, 2011.

[34] *J. Vila-Comamala et al.*, "High sensitivity X-ray phase contrast imaging by laboratory grating-based interferometry at high Talbot order geometry", Opt. Express, vol. 29, no. 2, pp. 2049-2064, Jan. 2021, doi: 10.1364/oe.414174.

[35] *N. Safca, D. Stutman, E. Anghel, F. Negoita, and C. A. Ur*, "Experimental demonstration of ultrahigh sensitivity Talbot-Lau interferometer for low dose mammography", Phys. Med. Biol., vol. 67, no. 23, article 23NT01, 2022, doi: 10.1088/1361-6560/aca514.

[36] *P. cheng Hu, D. Chang, J. bin Tan, R. tao Yang, H. xing Yang, and H. jin Fu*, "Displacement measuring grating interferometer: a review", Frontiers of Information Technology and Electronic Engineering, vol. 20, no. 5, pp. 631–654, May 01, 2019, doi: 10.1631/FITEE.1800708.

[37] *J. S. Yang, S. Y. Jeon, and J. H. Choi,* "Acquisition of a Single Grid-Based Phase-Contrast X-Ray Image Using Instantaneous Frequency and Noise Filtering", Biomed. Eng. Online, vol. 21, no. 1, Dec. 2022, doi: 10.1186/s12938-022-01061-z.